Chapter 4

# Investigation of Turbulence Models in the Analysis of Two Different Airfoils with Computational Fluid

**Mehmet Bakırcı**[1]

**Abstract**

Various standard airfoils are used in aviation, wind turbine blade designs, and for other applications that rely on aerodynamic forces. The rapid evolution of computing methods now allows you to accurately calculate the flow behavior of the airfoil in the short term. In this study, the aerodynamic performance of the NACA 63-215 and NACA 65-421 standard airfoils created by the National Aeronautics Advisory Committee (NACA) was analysed with two-dimensional computational fluid dynamics. These analyses were performed on a $1 \times 10^6$ Reynolds number and at different attack angles to discover better aerodynamic performance. Spalart-Allmaras, the standard k-ε and standard k-ω turbulence models are evaluated comparatively based on experimental data. Finally, the results and comparison of various properties i.e., drag and lift coefficients, pressure distribution over the airfoils are presented to help the user choose the right airfoil, and the turbulence model for a wing design or other aerodynamic modelling corresponds.

## 1. Introduction

Airfoil aerodynamics is a global field of study that has made a significant contribution to the growth of the wing and propeller industries. Airfoils and aerodynamically formed objects are widely utilized in a variety of aerial vehicles, including the aircraft, airplanes, helicopters and even rocket missiles. With regard to fluid machines like turbines, windmills, and pumps, the impeller and propeller shapes are particularly important. All of the critical parameters for representing the characteristics of the airfoils must be precisely regulated. This is due to the importance of flow analysis across an airfoil [1].

The aerodynamic performance of the airfoil is important for many applications. For example, aircraft aerodynamic performance affects factors

[1] Karabuk University Mechanical Engineering mehmetbakirci@karabuk.edu.tr

https://doi.org/10.58830/ozgur.pub130.c541

such as aircraft speed, range, and fuel economy. The aerodynamic performance of wind turbines affects the amount of energy produced by the turbines. The aerodynamic performance of vehicles affects fuel consumption and emissions [1].

Airfoil sections are designed to optimize aerodynamic performance. This helps create less resistance and produce more thrust or lift when moving over air or water. Airfoil sections can be designed at many different scales. This allows them to be used in different applications. For example, large-sized airfoil sections can be used for aircraft wings, while small-sized airfoil sections can be used for aircraft engine turbine blades. They are used in many areas in engineering designs. For instance, airfoil sections are used in the design of aircraft parts such as aircraft wings and horizontal stabilizers and are designed to optimize the airplane's effect on airflow. They are used in the design of wind turbine blades. They are also used in wind turbine blades to generate electrical energy by making more rotational movement under the influence of the wind. Airfoil sections are used in the design of vehicles in the automotive industry. In order to optimize the aerodynamic performance of the vehicles, they are utilized in the design of various vehicle parts such as windshield, rear glass, and rear spoiler. Additionally, airfoil sections are used in ship design. In the structure of the rudders positioned at the stern of the ship and on the sides of the deck. In order to reduce the effect of wind loads, especially for tall buildings, airfoil sections can be used in structural elements of buildings. As can be seen from these examples, airfoil sections are used in many engineering designs. The design and their use help to increase aerodynamic performance and to design more efficient systems. Airfoil sections can be produced from different materials. These materials can be chosen depending on the application's requirements and performance goals. Airfoil sections generally have smooth surfaces. This helps create less resistance and produce more thrust or lift when moving over air or water [1].

The moment coefficient of the airfoil is an important factor that measures the tendency of the flow around the airfoil to produce moment. It complements the aerodynamic properties of the airfoil, along with other coefficients such as torque coefficient, lift coefficient and drag coefficient. It is important as one of the factors affecting the aerodynamic performance of the airfoil, because the moment coefficient of the airfoil determines the aerodynamic moments that affect the balance and control properties of the airfoil. This affects the airfoil's horizontal stability and vertical control ability, roll moment, and other properties. It depends on factors such as

the size and shape of the airfoil, the angle of attack, and the Reynolds number. Moment coefficients help determine the stability and control characteristics of aircraft. Airfoil moment coefficients are also used in ship propeller design and many other applications. The stability performance of the airfoil depends on the aerodynamic moment coefficients of the airfoil and other factors and determines how the airfoil responds to changes in angle of attack or other external influences [2].

Previously, research on airfoil aerodynamics was limited to field testing, theoretical studies, and wind tunnel testing, all of which require significant work and money. Aerodynamic performance of airfoil sections might be evaluated using the finite element technique (FEM) used in computational fluid dynamics (CFD) for fluid flows, which has led to the creation of computer-assisted design programs. Numerical approaches for performance analysis and optimal design of an airfoil save money and time when compared to theoretical and experimental methods [3].

In general, airfoils are designed using one of two methods: First, make some tweaks to the real airfoils and repeat the procedure until improved performance is obtained. Second, identify the pressure coefficient distribution that will provide the desired aerodynamic performance and obtain the geometry that will produce this distribution. The National Advisory Committee on Aeronautics (NACA) performed an extensive variety of studies and tests on airfoil design. As a result, they developed their own standard airfoil section geometry series [2].

The NACA airfoil series, which is being used today, was created for World War II warplanes. The literature continues to investigate airfoils. Many researchers looked at the lift and drag presentation of NACA airfoils. To date, the following studies have been presented. S. Sarada et al. (2010) [4] used the ANSYS Fluent CFD tool to examine the NACA 64618 airfoil in 2D and 3D. They employed the k-epsilon turbulence model. With this model, they captured respectable values for the stall moment in 3D but not the same in 2D. A. Saraf et al. (2013) [5] investigated the aerodynamics of the NACA 4412 section using CFD and conventional k-epsilon and k-omega turbulence models. While they obtained comparable findings with studies at low attack angles by utilizing k-omega, the results at high angles were different with both models. D. Hartwanger and Dr. A. Horvat (2008) [6] used CFD, X-FOIL, and ANSYS CFX computer package tools to study the NREL S809 wind turbine blade section (airfoil). He performed a 2D flow study, employing laminar flow for the first half of the airfoil and turbulence for the rest. He demonstrated that the new model's conclusions were completely consistent with the experiments for the

circumstances prior to the stall. He did, however, state that the data obtained during and after the stall were incompatible with the trials. The lift and drag coefficients of the NACA 4412 airfoil were computed using CFD by H. C. Ravi et al. (2013) [7]. They picked the k-omega SST transition turbulence model to take into account the change of flow over an airfoil from laminar to turbulence and compared the findings produced by this model with the results obtained by the Spalart-Allmaras model and tests. They discovered concordance between both models and experiments at the end of the research. The mesh is the collection of small elements used to represent the fluid domain in the simulation.

E.C. Douvi et al. (2012) [8] evaluated turbulence models for modeling of flow over the NACA 0012 airfoil. J. Johansen (1997) [9] investigated the laminar/turbulent transition in airfoil flows. The numerical calculation of turbulent flows was emphasized by B.E. Launder and D. B. Spalding (1974) [10]. O. Gulzar et al. (2014) [11] used the Spalart-Allmaras turbulence model to simulate the effect of attack angle modification on the NACA 7420 airfoil in transonic compressible flow. NACA 4412 and NREL S 809 airfoils were compared by B.N. Kumar et al. (2016) [12]. The comparison of the NACA 4412 airfoil with the S 809 airfoil revealed that the NACA 4412 had superior aerodynamic performance over the whole spectrum of angles of attack. O. Badran (2008)[13] investigated a two-equation turbulence model that may forecast boundary layer separation on a NACA 4412 airfoil at a position of $\alpha=15°$. The developed turbulence model was proven to be capable of predicting the physics of unstable separated flow. The models provided results that were very close to the experimental data. G.E. Hassan et al. (2014) [14] determined the lift and drag coefficients of the NACA 0018 airfoil for angles of attack ($\alpha$) between $0^o$ and $25^o$ and Reynolds numbers from 300 000 to 1 000 000. When compared to experimental data in the literature for all tested ranges of Re values, the k– ω SST model yields the best correct predictions for lift coefficient ($C_L$) and drag coefficient ($C_D$).

The quality of the mesh can have a significant impact on the accuracy and reliability of the simulation results. Therefore, much research is focused on developing new methods to improve mesh quality. There are many different turbulence models, each with its own set of assumptions and limitations. Current studies in airfoil aerodynamics are focused on developing and refining turbulence models to improve their accuracy and reduce the computational cost of simulations. airfoil aerodynamics is a rapidly advancing field, with many exciting new developments and research opportunities [15].

In this work, two different National Advisory Committee on Aeronautics (NACA) airfoils, NACA 63-215 and NACA 65-421, are chosen for modeling of the flow field and the various turbulence models; Spalart-Allmaras, standard k-ε, and standard k-ω are used to obtain the aerodynamic coefficients. The results from the three different turbulence models are compared to reliable experimental results [16].

## 2. Mathematical Model

### 2.1. Flow Over an Airfoil

Airfoils are specially designed geometries that extract maximum lift while minimizing drag forces during air intake. These forces are generated by an airfoil due to pressure differences between its upper and lower surfaces. Drag is defined as the force exerted on an object in the flow direction. And the lift force may be expressed as a compound force that is vertical to the flow direction. Figure 1 describes the lift force, drag force and moment that occur around an airfoil section as a function of air speed [2].

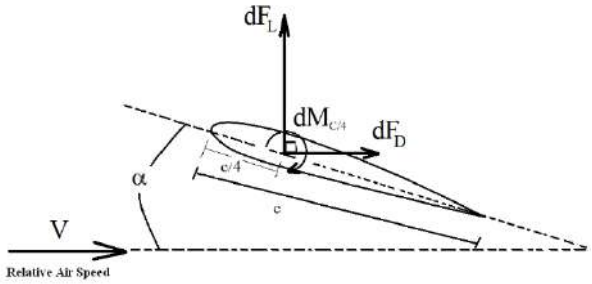


**Figure 1.** The factors on an airfoil.

When pressure (P) and shear (τ) forces apply on a differential surface area (dA), the differential lift and drag forces acting on dA are as follows:

$$dF_L = PdA\sin\theta - \tau dA\cos\theta \quad (1)$$

$$dF_D = PdA\cos\theta + \tau dA\sin\theta \quad (2)$$

From Eqns. 3 and 4 we can calculate the lift and drag coefficients that occur,

$$C_L = \frac{dF_L}{\frac{1}{2}\rho V^2 cdr} \quad (3)$$

$$C_D = \frac{dF_D}{\frac{1}{2}\rho V^2 c dr} \quad (4)$$

$$C_M = \frac{dM}{\frac{1}{2}\rho V^2 c^2 dr} \quad (5)$$

Where the variables are shown in Table 1.

**Table 1.** Nomenclatures of Eqns. 3, 4.

| Symbol | Name | Unit |
|---|---|---|
| $C_L$ | *coefficient of lift* | - |
| $C_D$ | *coefficient of drag* | - |
| $dF_L$ | *partial lift force* | N |
| $dF_D$ | *partial drag force* | N |
| dM | *partial moment* | Nm |
| V | *wind speed* | m/sec |
| c | *chord* | m |
| dr | *partial width of the blade element* | m |

As the airflow passes over an airfoil, the speeds of the air molecules change. Since the upper surface is humped, the speed increases when passing over it and decreases when passing over the lower surface. While the static pressure increases on the lower surface where the velocity decreases, it decreases on the upper surface where the velocity increases. This pressure difference, which occurs on the lower and upper surfaces of the airfoil, causes the lift force [2].

The lifting phenomena may also be described using the Bernoulli equation. Based on Bernoulli's equation, pressure rises as flow velocity falls in an incompressible steady-state flow, and vice versa. So, we can observe that when the air goes over the airfoil, the velocity increases as it flows from the leading edge to the top surface, decreasing the pressure in that region. On the other hand, when air flows through the bottom of the airfoil, pressure rises even while velocity falls. Upward positive pressure is the most important factor in creating lift [2].

When a moving liquid separates from a body, a separated region forms between the object and the air flow. The split region is a low-pressure area behind the body that is subject to re-circulation and back-flows. The size of the separated field determines the drag force. The word "wake" refers to a

flow region trailing the body where the velocity impacts of the body may be sensed. Vortexes in the wake creates drag by creating negative pressure in the area. Wake does not occur with bluff bodies. Wake may arise in an aerodynamic body. This angle of attack is slightly larger than 15 degrees for most airfoils. This is known as a stalling point (Fig 2.)[2].

The stability of the airfoil is calculated by determining the aerodynamic moment coefficients and the aerodynamic center position. Aerodynamic moment coefficients measure the tendency of the flow around the airfoil to produce moment (torque), while the aerodynamic center position is the point where the aerodynamic moment coefficients of the airfoil change according to the lift coefficient change. Stability performance is measured by two types of stability: static stability and dynamic stability. While static stability measures the airfoil's response to changes in angle of attack, dynamic stability measures how the airfoil behaves in a moving environment. The stability performance of the airfoil depends on the aerodynamic moment coefficients, aerodynamic center position and other factors. These factors depend on various parameters such as the size and shape of the airfoil, angle of attack and Reynolds number. The stability performance of the airfoil is important in aircraft design and many other applications because it is an important factor determining the safety and control characteristics of the airfoil [2].

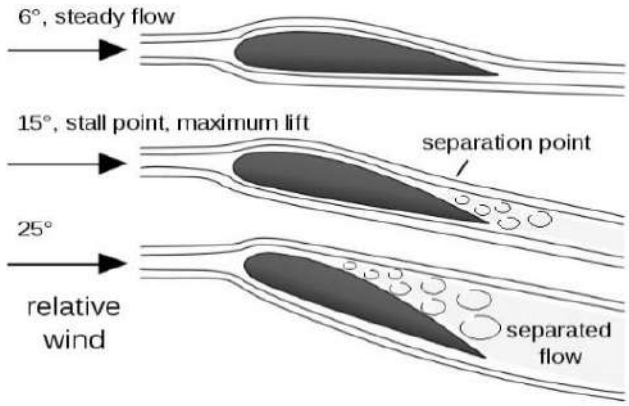


**Figure 2.** Flow separation on an airfoil.[2]

The curves of the airfoils drawn by the standard coordinates which the study uses, NACA 63-215 and NACA 65-421 are shown in Figures 3 and 4. [16]

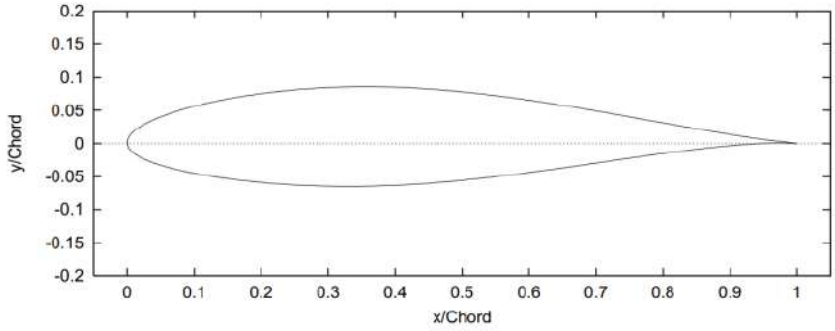


**Figure 3.** The airfoil section curve of NACA 63-215.

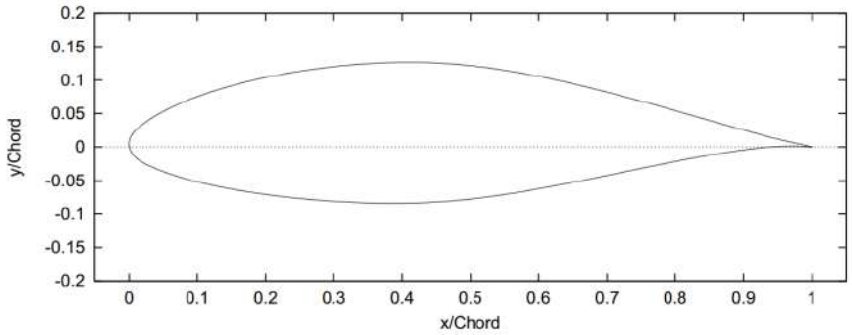


**Figure 4.** The airfoil section curve of NACA 65-421.

NACA airfoil designation provides information about the key geometric features of the airfoil, including the maximum camber and thickness, which is useful in aerodynamics analysis and design. For the case of NACA, NACA 63-215 and NACA 65-421, the numbers "63" and “65” respectively refer to the location of the maximum camber in percentage of the chord length (63% and 65% from the leading edge) while the numbers "2" and “4” respectively refer to the maximum camber in percentage of the chord length (2% and 4% of the chord length). The numbers “15” and "21" respectively refer to the maximum thickness of the airfoil in percentage of the chord length (15% and 21% of the chord length) [1].

The NACA 63-215 and NACA 65-421 airfoils are primarily designed for subsonic flow applications, which means they are most suitable for vehicles that operate at relatively low speeds, such as general aviation aircraft, drones, and small wind turbines.

### 2.2. Computational Fluid Dynamics (CFD)

Airfoil (airfoil profile) can be examined with CFD analyses to determine its aerodynamic performance. During the analysis, the following issues can be examined; The flow field around the airfoil can be studied in detail by CFD analysis. This analysis is performed by considering variables such as airflow rate, pressure, temperature and other flow characteristics. The pressure distribution on the airfoil can be calculated in detail by CFD analysis. This provides information on the aerodynamic performance of the airfoil and can be used to optimize it. The frictional forces on the airfoil can be calculated by CFD analysis which is important for understanding the factors that affect the resistance of the airfoil and its aerodynamic performance. The lift coefficient of the airfoil can be calculated by CFD analysis which is crucial for determining the aerodynamic performance of the airfoil and can help optimize the design of the airfoil. The aerodynamic noise around the airfoil can be calculated by CFD analysis. This is important for making design changes to reduce noise on airplanes. CFD analysis of the airfoil is important for understanding and optimizing the aerodynamic performance of the airfoil. These analyses are used in aircraft design, wind turbines, vehicle design and many other applications [3].

Reynolds Averaged Navier-Stokes (RANS), Large Eddy Simulation (LES), Detached Eddy Simulation (DES) and Direct Numerical Simulation (DNS) models used in computational fluid dynamics are designed for simulation of different flow events. RANS approaches model turbulence behavior by averaging over time, providing accurate results on the average flow behavior. However, these models cannot model natural turbulence events and there is a possibility of serious error. Therefore, they are mostly used in industrial applications. LES models accurately capture large-scale turbulent structures and model small-scale structures. Therefore, LES models are used to simulate natural turbulence events. However, these models are generally used in a limited number of research applications due to their high computational cost. DES models are a combination of RANS and LES models. Models employ the LES method to capture large-scle structures and the RANS method to model small-scale structures. Therefore, DES models provide more accurate results for industrial applications. DNS models resolve all scales of the flow. Hence, DNS models provide the most accurate results. However, these models are the most computationally costly and are used only in small-scale research applications. Therefore, the selection of the right turbulence model depends on the nature of the simulated flow event, accuracy and computational cost. Industrial applications often use RANS or DES models, while research applications may use LES or DNS models [17].

Turbulence models used in computational fluid dynamics (CFD) applications are essential to accurately predict fluid motion. Different turbulence models try to model the effect of turbulence using different approaches. Simpler models often come with less computational costs, but are less accurate. More complex models tend to produce more accurate results, but the computational cost may be higher. Some models are only suitable for certain types of flows, while others can be used for a wider range. Whether the models are compatible with experimental data can also be a comparison criterion [18].

Turbulence models used in computational fluid dynamics (CFD) simulations provide solutions by mathematically modelling the turbulent motion of fluids. The k-epsilon, k-omega and Spalart-Allmaras models are three different turbulence models frequently used in CFD. The k-epsilon model is used to calculate the balance between turbulent kinetic energy (k) and dissipated energy (epsilon). This model gives good results in smooth flows and adiabatic walls, but it may not be accurate in pressurized surfaces and high sections. The k-omega model was developed to overcome the disadvantages of the k-epsilon model. This model requires less computation than the k-epsilon model and gives better results at low Reynolds number flows. However, it may not give accurate results on pressurized surfaces. The Spalart-Allmaras model is used to determine the viscosity of turbulent flow. This model gives good results at high Reynolds number flows and pressure surfaces. It also requires fewer iterations than other models. However, it cannot give accurate results in various flow conditions, such as turns in flow. As a result, each turbulence model offers advantages and disadvantages in different flow conditions. To obtain accurate results, the turbulence model to be applied should be chosen according to the characteristics of the flow, the Reynolds number, and the purposes of the analysis [19, 20].

The k-epsilon turbulence model is a turbulence model frequently used in CFD simulations and has various sub-models. The most common sub models are: Standard k-epsilon model: This model is used to calculate the balance between turbulent kinetic energy (k) and dissipated energy (epsilon). It performs well in smooth flow conditions, but may give inaccurate results on pressurized surfaces and high cross sections. Realizable k-epsilon model: This model was developed to overcome the disadvantages of the standard k-epsilon model. The realizable k-epsilon model uses a realistic set of equations to calculate the Reynolds stress tensor. This model gives more accurate results on pressurized surfaces and high sections. RNG k-epsilon model: This model was developed by

Richardson and Nicoud and uses the balance between turbulent kinetic energy (k) and dissipated energy (epsilon) instead of directly calculating the Reynolds stress tensor. This model gives good results for high Reynolds number flows and complex geometries. Nonlinear k-epsilon model: This model uses a nonlinear set of equations to calculate the balance between turbulent kinetic energy (k) and dissipated energy (epsilon). This model gives more accurate results on pressurized surfaces and high sections.

These sub models include different approaches to turbulence kinetics and offer different mathematical solutions to better adapt to different flow conditions [21] .

The k-omega turbulence model is a turbulence model used to calculate the relationship between turbulent kinetics and turbulent viscosity. The most common sub models of this model are: Standard k-omega model: This model uses a transport equation to calculate turbulent viscosity and defines a new variable called omega as a function of turbulent kinetics. It performs well in smooth flow conditions, but may give inaccurate results on pressurized surfaces and high cross sections. SST (Shear Stress Transport) k-omega model: This model was developed to overcome the disadvantages of the standard k-omega model. The SST k-omega model gives better results than the standard k-omega model under smooth flow conditions and gives more accurate results on pressurized surfaces and high sections. BSL (Baldwin-Lomax) k-omega model: This model was developed to perform better at low Reynolds number flows. The BSL k-omega model gives better results than the standard k-omega model on pressurized surfaces and high sections. These sub models use different mathematical equations for the calculation of turbulent viscosity and offer different approaches to better adapt to different flow conditions [22].

The Spalart-Allmaras (SA) turbulence model is a single-equation turbulence model and uses a single variable, turbulent viscosity, rather than turbulence kinetics. There are no sub models of the SA model. However, modifications and updates of the SA model are in progress. For example, the Spalart-Allmaras-DDES (Detached-Eddy Simulation) model is a model developed based on the SA model. This model performs better in simulating high Reynolds number flows and gives more accurate results due to the combination of the turbulence model and the eddy-viscosity model. Similarly, the Spalart-Allmaras-IDDES (Improved Detached-Eddy Simulation) model is an improved version of the SA model and gives more accurate results in simulating high Reynolds number flows [23].

When choosing turbulence models, some factors should be taken into account in order for the calculations to give accurate results and reflect the flow behaviors observed in real life. Pressurized or unpressurized flow, turbulence level and Reynolds number play an important role in turbulence model selection. According to the purpose of the calculations, the choice of turbulence model may vary. For example, RANS models can be used if the flow needs to be examined in detail, while LES or DNS models can be preferred for highly turbulent flows. Sufficient data for the geometry or flow to be calculated is important in turbulence model selection. For example, some turbulence models may require smooth geometry. The accuracy of turbulence models is important so that calculations give accurate results and reflect real-life flow behavior. Therefore, the accuracy of the turbulence model should be compared with the data in the literature and its suitability should be tested. Some turbulence models give more accurate results by increasing the computation time, while others require less computation time but give less accurate results. Considering these factors, turbulence model selection should be made. Also, by comparing the results of different turbulence models, it can be determined which model is the most suitable [24].

Experiments, theoretical formulae, or CFD can be used to compute the occurrence of aerodynamic force coefficient values as they flow across an airfoil. Because of the exceptions based on theoretical calculations, the obtained numbers are only approximations. Experiments can produce more reliable findings; however, the flow separation of stall moments reduces dependability [25].

CFD, on the other hand, provides rapid and consistent results for the force and coefficient values that occur around an airfoil. However, the flow physics, cell formation mechanism, and selection of the appropriate turbulence model all have a direct impact on the accuracy of the results [26, 27].

Many commercial CFD software packages are used in engineering. The primary simulation procedure is the same regardless of the type of CFD software utilized. Setting up governing equations is a prerequisite for CFD modelling; the three fundamental governing equations are mass, momentum and energy conservation equations. Following that, boundary conditions are defined based on various flow circumstances, and a mesh is formed. The meshing model's objective is to discretize equations and boundary conditions into a single cell. A cell is the fundamental building block of both organized and unstructured networks. While tetrahedral and pentahedral cells are often employed in unstructured grids, hexahedral cells

are utilized in organized grids. The mesh quality is necessary for obtaining appropriate physical solutions, and it is up to the engineer's competence. The more nodes in the mesh, the longer it takes to solve the aerodynamic issue, hence, developing an efficient mesh is critical [18].

CFD is a mathematical model based on Euler or Navier-Stocks that provides a consistent and physically accurate simulation of the flow field and may naturally be used to solve the complicated flow over an airfoil. The simulation approach of Reynolds-Averaged Navier-Stokes (RANS) is widely employed [17].

Two dimensional Navier Stokes equations include one continuity (Eqn. 5) and two momentum conservation (Eqns. 6, 7) equations:

$$\frac{\partial u}{\partial x} + \frac{\partial v}{\partial y} = 0 \tag{5}$$

$$\rho u\frac{\partial u}{\partial x} + \rho v\frac{\partial u}{\partial y} = \frac{\partial p}{\partial x} + \frac{\partial}{\partial y}\left[\mu\left(\frac{\partial v}{\partial x} + \frac{\partial u}{\partial y}\right)\right] + \frac{\partial}{\partial x}\left(-\rho\overline{u'v'}\right) \tag{6}$$

$$\rho u\frac{\partial v}{\partial x} + \rho v\frac{\partial v}{\partial y} = \frac{\partial p}{\partial y} + \frac{\partial}{\partial x}\left[\mu\left(\frac{\partial v}{\partial x} + \frac{\partial u}{\partial y}\right)\right] + \frac{\partial}{\partial y}\left(-\rho\overline{u'v'}\right) \tag{7}$$

While the right side of the equation expresses average body force and divergence stress, the left side of the equation explains the change in mean momentum. In these equations, u and v define velocity components in the x and y directions, respectively, p represents pressure, μ dynamic viscosity, ρ fluid density, and u' and v' represent horizontal and vertical turbulence speed deviation. -ρu'v' is turbulent shear stress, denoted as $\tau_{xy}$ and derived using the Eqn. 8 formula:

$$\tau_{xy} = -\rho\overline{u'v'} = \eta\left(\frac{\partial u}{\partial y} + \frac{\partial v}{\partial x}\right) \tag{8}$$

Where η is called turbulence viscosity, and many turbulence models have been created to determine it (Anderson J. D., 1995) [3]. Because RANS equations are open owing to the inclusion of a stress factor, a turbulence model is required to generate a closed system of a solvable solution. Many turbulence models are employed today, including algebraic, single-equation, two-equation, and Reynolds stress models. The majority of turbulence models used are Spalart-Allmaras turbulence, k-ε turbulence and k-ω turbulence models. There is no single optimum turbulence model

that applies to all flows. If required, the results acquired using multiple models for the same flow should be compared, especially with low wind speeds (Mach number<<1) at attack angles before stall since found result values are quite near to each other [28].

### *2.2.1 The Spalart-Allmaras turbulence model*

The Spalart-Allmaras turbulence model is a one-equation model that solves a modelled transport equation with kinematic eddy (turbulent) viscosity (1992). It was developed particularly for aerospace applications having especially wall-bounded flows, and it has been demonstrated to provide appropriate results for boundary layers subjected to unfavorable pressure gradients. It's also becoming more popular in turbomachinery. In its original form, it is simply a low-Reynolds number model that necessitates precise resolution of the viscous-affected portion of the boundary layer. The gradients of the conveyed variable in the model are significantly less than those in the k-ε or k-ω models. The transport equation of the Spalart-Allmaras turbulence model can be stated in the operational parameter v~, as shown below [20]:

$$\frac{D\tilde{v}}{Dt} = c_{b1}(1-f_{t2})\tilde{S}\tilde{v} + \frac{1}{\sigma}\left[\nabla.\left((v+\tilde{v})\right)\nabla\tilde{v} + c_{b2}(\nabla\tilde{v})^2\right] - \left(c_{w1}f_w - \frac{c_{b1}}{K^2}f_{t2}\right)\left(\frac{\tilde{v}}{d}\right) + f_{t1}\Delta U^2 \qquad (9)$$

Sutherland's (1893) method is used to compute v, which is the chemical viscosity. The four words on the right-hand side are, in order, production, diffusion, dissipation, and transformation. Individual components of the production term are as follows: (2021):

$$f_w = \frac{\tilde{v}}{\tilde{S}k^2d^2}\left[1 + C_{w2}\left(\left(\frac{\tilde{v}}{\tilde{S}k^2d^2}\right)^5 - 1\right)\right](1 + C_{w3}^6)^{1/6}\left\{\left[1 + C_{w2}\left(\left(\frac{\tilde{v}}{\tilde{S}k^2d^2}\right)^5 - 1\right)\right]^6 + C_{w3}^6\right\}^{-1/6} \qquad (10)$$

$$f_{t1} = C_{t1}g_t \exp\left[-C_{t2}\frac{\omega_t^2}{\Delta U^2}(d^2 + g_t^2 d_t^2)\right], f_{t2} = C_{t3}\exp\left[-C_{t4}\left(\tilde{v}/v\right)^2\right] \qquad (11)$$

In these equations, $S$ is the value of the vorticity, $d$ is the distance to the closest wall, $d_t$ is the distance from the point in the flow field to the trip on

the wall, $\omega_t$ is the wall vorticity at the trip, $\Delta U$ is the difference between velocity at the field point and that at the trip, $g_t = min\ (0.1,\ \Delta U/\omega_t \Delta x_t)$ where $\Delta x_t$ is the grid spacing along the wall at the trip.

The empirical constants in the Spalart-Allmaras model are: $C_{b1} = 0.1355$, $\sigma = 2/3$, $C_{b2} = 0.622$, $k = 0.4187$,

$C_{w1} = 3.239$, $C_{w2} = 0.3$, $C_{w3} = 2.0$, $C_{v1} = 7.1$, $C_{t1} = 1$, $C_{t2} = 2$, $C_{t3} = 1.2$ and $C_{t4} = 0.5$.

### *2.2.2 The standard k-ε turbulence model*

The standard k-ε turbulence model equations account for the contribution of the change in average speed and the lift force in creating turbulence kinetic energy and swashes, which are compressible at all spread rates and expandable in the turbulence. The following transport equations, Chan et al., (2002) [29] are used to calculate the turbulent kinetic energy, k, and rate of dissipation, ε:

$$\frac{\partial(\rho k)}{\partial t} + \frac{\partial(\rho k u_j)}{\partial x_j} = \frac{\partial}{\partial x_j}\left[(\mu + \frac{\mu_t}{\sigma_k})\frac{\partial k}{\partial x_j}\right] + G_k + G_b - \rho\varepsilon \quad i,j = 1,3 \qquad (12)$$

$$\frac{\partial(\rho \varepsilon)}{\partial t} + \frac{\partial(\rho \varepsilon u_j)}{\partial x_j} = \frac{\partial}{\partial x_j}\left[(\mu + \frac{\mu_t}{\sigma_\varepsilon})\frac{\partial \varepsilon}{\partial x_j}\right] + C_{1\varepsilon}\frac{\varepsilon}{k}(G_k + C_{3\varepsilon}G_b) - C_{2\varepsilon}\rho\frac{\varepsilon^2}{k} \quad i,j = 1,3 \qquad (13)$$

The turbulent (or eddy) viscosity, $\mu_t$, is computed by combining $k$ and $\varepsilon$ as follows:

$$\mu_t = \rho C_\mu \frac{k^2}{\varepsilon} \qquad (14)$$

Where $G_k$ is the turbulence kinetic energy production. It is due to the change in average velocity. $G_b$ indicates the turbulence kinetic energy production caused by the buoyancy force.

In this study, as the experimental data of k-epsilon turbulence model, $C_{1\varepsilon} = 1.44$, $C_{2\varepsilon} = 1.92$, $C_\mu = 0.09$, $\sigma_\varepsilon = 1.3$, $\sigma_k = 1$ values were used [21].

### *2.2.3 The standard k-ω turbulence model*

The standard k-ω turbulence model is an empirical model that is relied on the transport equations related to turbulent kinetic energy (k) and particular dissipation rate (ω). It may alternatively be regarded as the ratio of ε to k. This model is developed on the Wilcox k-ω model, which has been modified to account for low-Reynolds-number effects, compressibility, and shear flow spreading.

The turbulence kinetic energy, $k$, and the specific dissipation rate, $\omega$, are obtained from the following transport equations [22],

$$\rho\frac{\partial k}{\partial t}+\ \rho u_j\frac{\partial k}{\partial x_j}=\frac{\partial}{\partial x_j}\left[(\mu+\sigma^*\mu_t)\frac{\partial k}{\partial x_j}\right]+G_k-\rho\beta^*k\omega \quad i,j=1,3 \tag{15}$$

$$\rho\frac{\partial \omega}{\partial t}+\ \rho u_j\frac{\partial \omega}{\partial x_j}=\frac{\partial}{\partial x_j}\left[(\mu+\sigma\mu_t)\frac{\partial \omega}{\partial x_j}\right]+\alpha G_k\frac{\omega}{k}-\rho\beta\omega^2 \quad i,j=1,3 \tag{16}$$

In these equations, $G_k$ is the turbulent kinetic energy production. $\sigma$, $\sigma^*$, $\alpha$, $\beta$, and $\beta^*$ are constants of values 1/2, 1/2, 5/9, 3/40, and 9/100, respectively. The turbulent viscosity, $\mu_t$, is computed by combining $k$ and $\omega$ by following equation [22]:

$$\mu_t=\rho\frac{k}{\omega} \tag{17}$$

## 3. Methodology

In the software, the CFD package solves three basic equality equations: mass, momentum, and energy conservation. Flow and flow field characteristics define boundary conditions. The flow field is segmented into cells (mesh). In these cells, these three conservation equations are solved along with boundary conditions. Cells in two-dimensional fields can be structured quadratic or unstructured triangular, as seen in Figure 5.

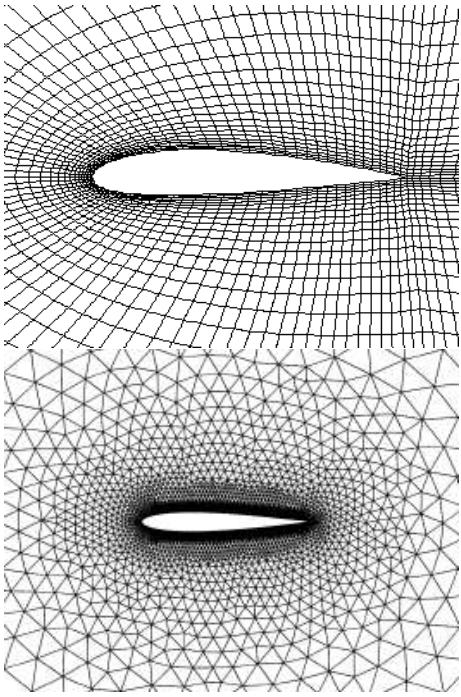

**Figure 5.** **(a)** Structured quadratic mesh grid; **(b)** Unstructured triangular mesh grid.

Triangular meshes can represent complex geometries more easily than quadrilateral meshes. Triangles can be used to represent curved boundaries and irregular shapes, and they can also be easily refined in regions where higher resolution is required. Triangular meshes may require more computational resources to achieve the same level of accuracy as a quadrilateral mesh. This is because triangular elements have fewer nodes than quadrilateral elements, which can lead to a higher number of elements required to represent a given geometry. Quadrilateral meshes can be more efficient computationally than triangular meshes. This is because quadrilaterals have more nodes than triangles, which means that fewer elements are required to represent a given geometry. Quadrilateral meshes may not be able to represent complex geometries as easily as triangular meshes. Quadrilaterals are generally less flexible than triangles in terms of their ability to represent curved boundaries and irregular shapes.

The precise division of cells is critical for obtaining accurate physical findings. While using fewer cells might result in incorrect findings, using too many cells necessitates high-capacity computers and additional time. Therefore, it is important to determine the optimal cell number.

Aerodynamic evaluations of NACA 63-215 and NACA 65-421 conventional wing section geometries were performed at various attack angles of flow conditions. As angle of attacks, 0 degrees, 10 degrees, and 20 degrees were employed. The length (c) of the wing section beam (chord) has been set at 1m. The velocity and pressure changes occurring about the two airfoils have been investigated and $C_L$ lift $C_D$ drag coefficients were calculated. These operations have been performed in the following order:

1. The airfoil coordinates were entered into a CAD computer, and two-dimensional geometries were generated.

2. The flow field geometry shown in the Figure 5 was created, and the limits of the flow region around the airfoil are depicted in Figure 6. Curve F and line C have been designated as the inlet and outlet, respectively, and the airfoil (curve G) has been designated as the 'wall.' As symmetry, AB and DE edges have also been introduced.

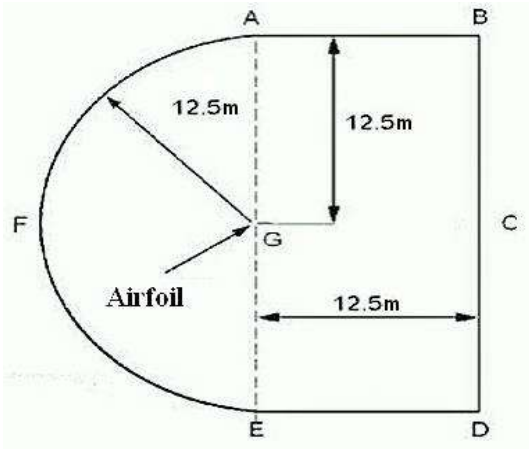


**Figure 6.** The flow domain, boundaries and dimensions.

3. After entering this geometry, including the wing cross-section (airfoil) and flow area, into the mesh software, the flow area was separated into cells (meshes). As illustrated in Figure 7, smaller cells on the surface of the airfoil and increasing cells by moving away from the geometry were generated. Each cell may be thought of as an infinitely small control volume in which the conservation equations are solved. CFD solution accuracy is determined by the size of the mesh grid. In this investigation, about 10 000, 107 000, and 1 500 000 triangular meshes were employed. However, after

100 000 meshes, it was discovered that the findings did not change much, therefore this mesh count was used throughout the research. Furthermore, it can be shown that the mesh metrics are of high quality.

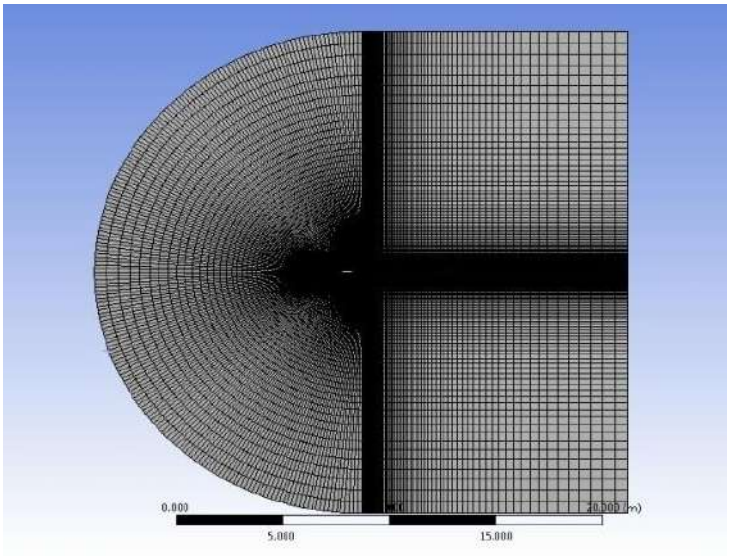


**Figure 7.** Meshed flow domain.

4. After the meshing procedure was completed, the flow domain geometry was imported into the CFD solution and the boundary conditions were established, as illustrated in Table 2.

**Table 2.** Boundary conditions

| Boundary Conditions | Choices |
|---|---|
| Simulation Type | Steady Simulation |
| Fluid | Air |
| Flow Type | Incompressible flow |
| Temperature | 300 K |
| Kinematic Viscosity | $1.4607 \times 10^{-5}$ $m^2/s$ |
| Pressure | 101325 pa. |
| Wind Speed | 20 m/s |
| CFD Algorithm | SIMPLE |
| Turbulent model | For each simulation respectively; Spalart-Allmaras, k-ε and k-ω |

| | |
|---|---|
| Solution Methods | Pressure-Velocity Coupling<br>Least Squares Cell Based<br>Pressure (Standard) Density<br>Momentum<br>Turbulent Kinetic Energy<br>Specific Dissipation Rate |
| Solution Controls | Pressure: 0.5<br>Momentum: 0.5<br>Density: 1.1 kg/m^3<br>Turbulent Kinetic Energy: 0.75 |
| Boundary Conditions | Velocity Inlet (20 m/s) and Pressure Outlet (gage pressure: 0) |
| Mesh Cells | Around 100000 |

5. The conservation equations and turbulence models are repeatedly solved for all cells starting with initial values. For iterations, the convergence criterion has been set at $10^{-6}$.

## 4. Results and Discussion

The aerodynamic efficiency of the airfoils was evaluated at different angles of attack. The experimental results were compared to the results obtained by using Spalart-Allmaras, k-ε, and standard k-ω turbulence models.

Figures 8 and 9 show the lift coefficient values for these two airfoil sections. The stall angle is the angle at which the coefficient of lift decreases with increasing angle of attack. In Figure 8, for NACA 63-215, while all models yield near results to the experimental data before stall, only Spalart-Allmaras approaches the experimental results after stall. In Figure 9, the k-ε turbulence model nearly matches the experimental data before and after stall for NACA 65-421.

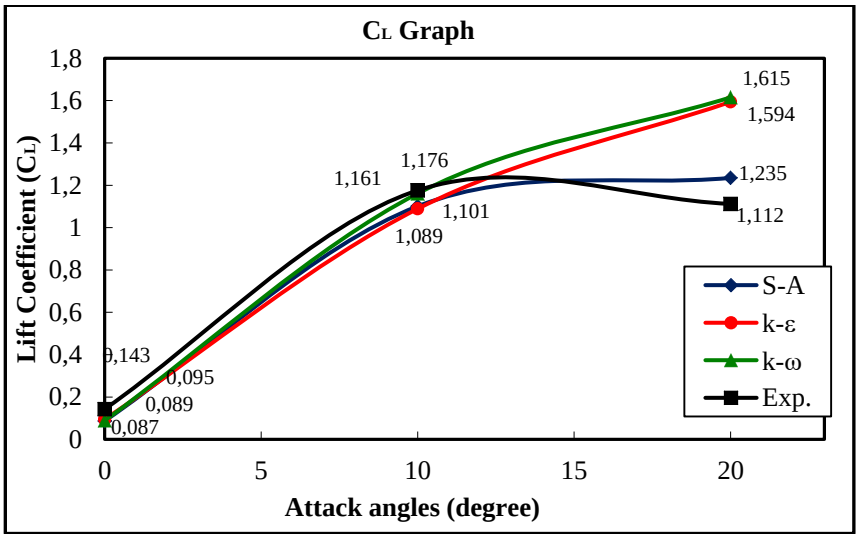


**Figure 8.** Lift coefficient comparison of NACA 63-215.

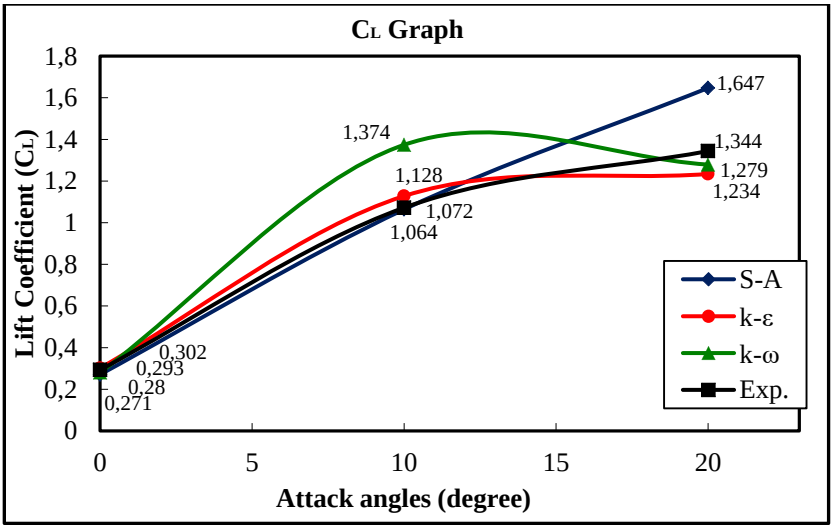


**Figure 9.** Lift coefficient comparison of NACA 65-421.

Figures 10 and 11 show the drag coefficient values for the various airfoil sections. In Figure 10, the estimated drag force for NACA 63-215 is somewhat greater than the experimental data before stall, but lower after stall. In Figure 11, whereas the other models miss the experimental data for NACA 65-421, the S-A turbulence model almost captures it before and after stall.

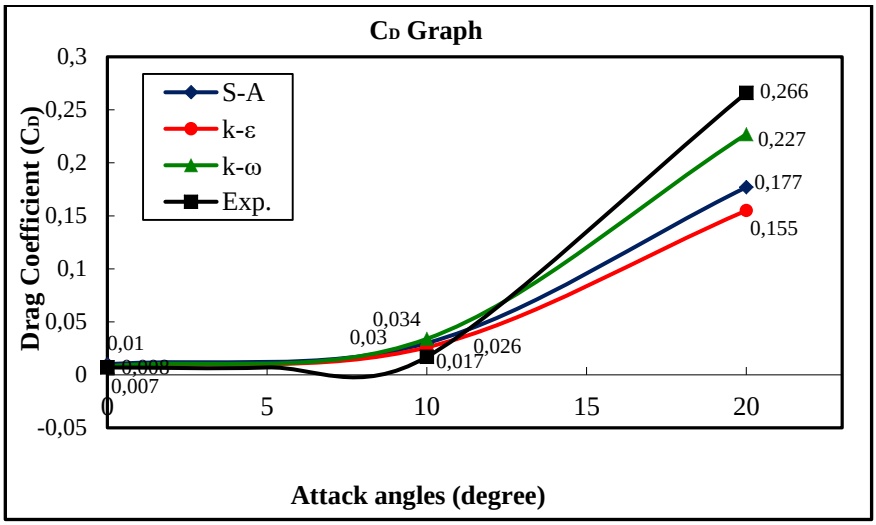


**Figure 10.** Drag coefficient comparison of NACA 63-215.

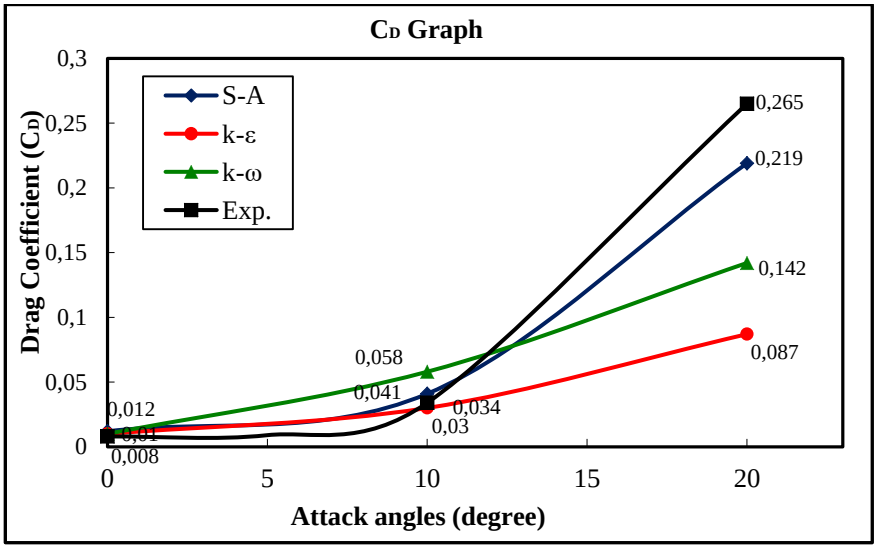


**Figure 11.** Drag coefficient comparison of NACA 65-421.

If we want to enhance aerodynamic performance, we should increase lift force while decreasing drag force. When the data in Figures 8, 9, 10, and 11 are taken into consideration, the lift/drag ratio is determined, as illustrated in Figures 12 and 13. In Figure 12, for NACA 63-215, while the predicted findings are closer to the experimental results at 0 and 20 attack angles, all models fail with substantially lower data at 10 degrees. In

Figure 13, for NACA 65-421, while all models have far results before stall, the S-A model has a closer result to the experimental data after stall.

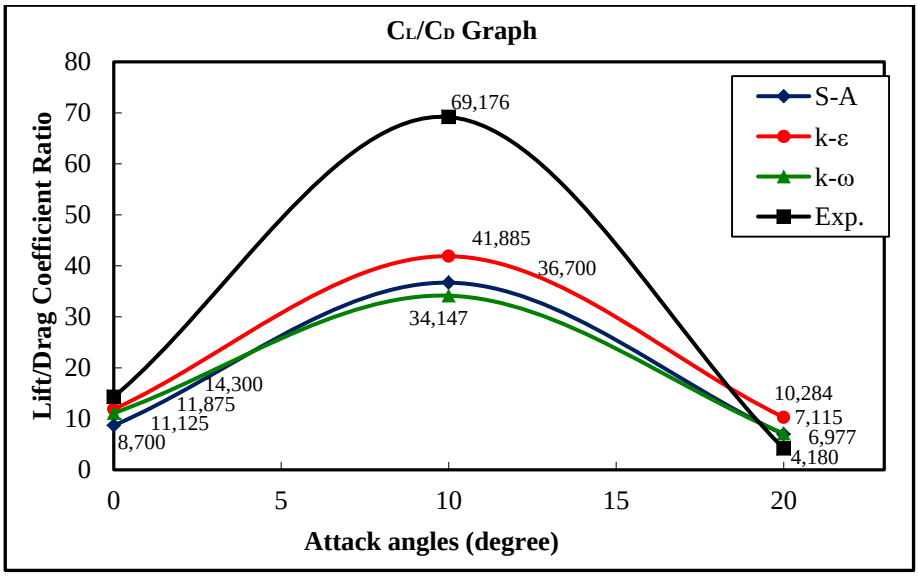


**Figure 12.** Lift/Drag coefficient ratio comparison of NACA 63-215.

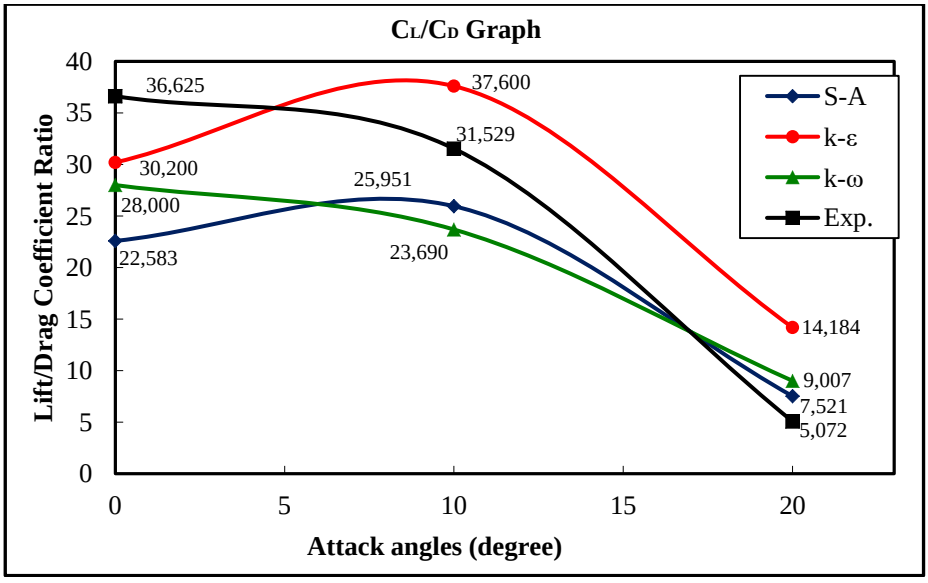


**Figure 13.** Lift/Drag coefficient ratio comparison of NACA 65-421.

One of the ways to understand the properties of flow around an object is to examine the pressure coefficient graph. The pressure coefficient takes

values that change from every point on the object to every point. This coefficient value is obtained by dividing the pressure value (which is the difference between the static pressure value at a certain point on airfoil surface and the static pressure value in the free region) by the dynamic pressure value in the free region. By looking at the graphs showing the changing values of the static pressure coefficient values according to the position on the upper and lower surfaces of the airfoil, it is possible to analyze the magnitude of the lift force and how it changes on the airfoil. Table 3 shows the pressure coefficient graphs obtained as a result of computational fluid dynamics analysis. The graphs obtained with Spalart Allmaras, k-epsilon and k-omega turbulence models for NACA 63-215 and for NACA 65-421 airfoils at 0, 10 and 20 degrees are shown comparatively in Table 3. The static pressure coefficient has different values at each point on the solid body surface around which there is flow. For this reason, static pressure graphs formed on the airfoil are drawn. These graphs are used to analyse the aerodynamic performance of the airfoil. As the area of the closed region formed in the static pressure coefficient graphs increases, the buoyant force value also increases. The static pressure values at each position at the top of an airfoil section are less than those at the bottom. Thus, lift and drag forces are results of the pressure difference of the pressure and suction sides of a body. There is more lift force where there is less pressure on the top section and more pressure on the bottom part.

**Table 3.** Pressure coefficient graphs of the airfoils.

| **Pressure Coefficient** | **NACA 63-215** | **NACA 65-421** |
|---|---|---|
| **0° Spalart-Allmaras** | 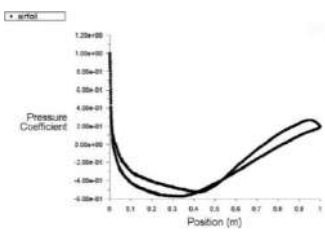 | 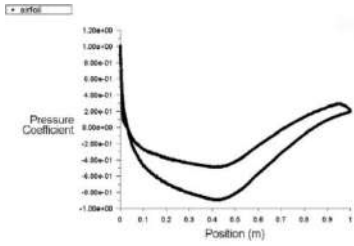 |

**0°**
**k-ε**

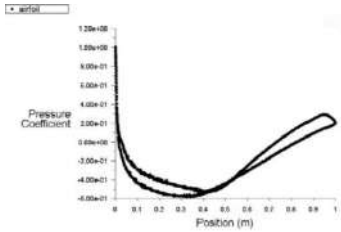


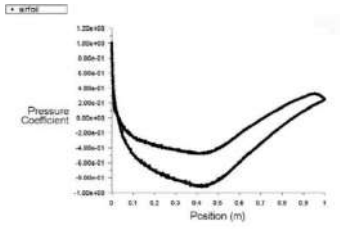


**0°**
**k-ω**

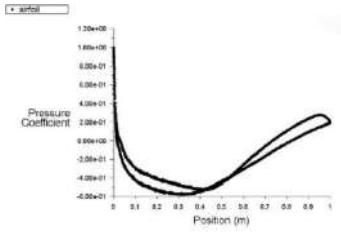


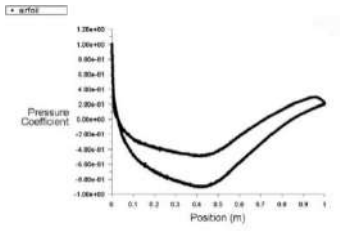


**10°**
**Spalart-**
**Allmaras**

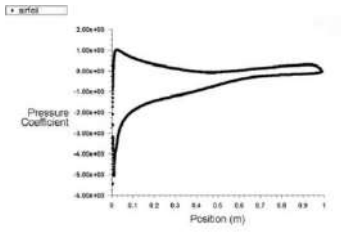


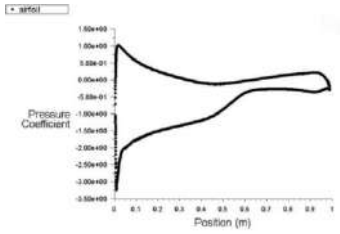


**10°**
**k-ε**

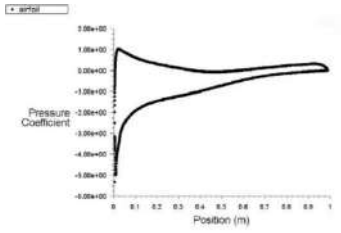


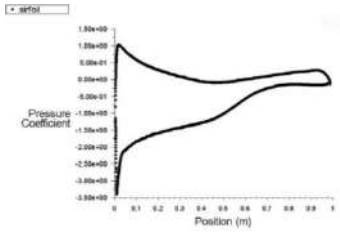


**10°**
**k-ω**

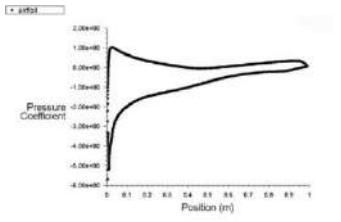


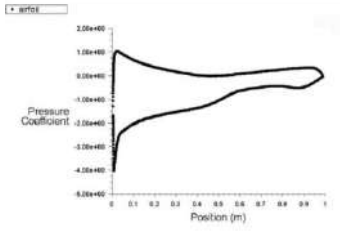

**20° Spalart-Allmaras**

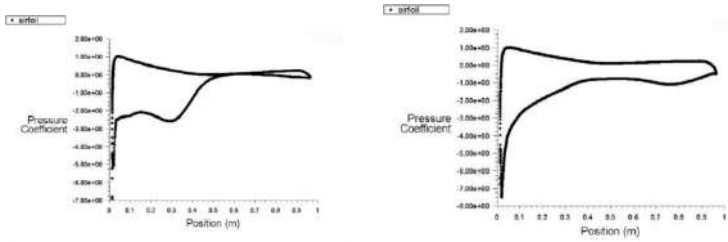


**20° k-ε**


**20° k-ω**

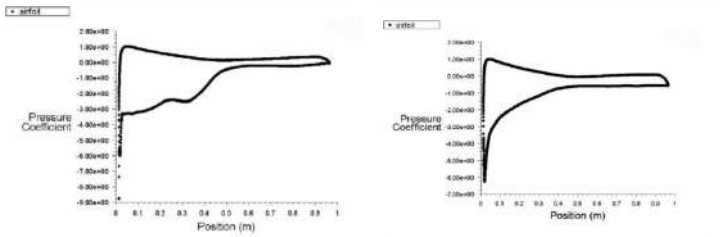


Table 3 compares the pressure coefficient graphs of the airfoils. The size of the closed regions between the upper and lower curves on the table graphs is related to the lift force. This region is greater than NACA 63-215 at NACA 65-421 cross section for all models. As a result, the lift force is greater. The same thing happens when the angle of attack rises: as the angle grows, so does the area.

For NACA 63-215, the position of the minimum static pressure coefficient value on the airfoil is 0.35c, 0.01c and 0.02c from the leading edge at zero degrees, 10 degrees and 20 degrees attack angles, respectively. For NACA 65-421, these values are 0.42c, 0.01c and 0.02c in the same order. These values are the same in all turbulence models. However, the minimum static pressure coefficient values were different for both airfoils and turbulence models. For NACA 63-215, the values found in three different turbulence models (S-A, k-epsilon, k-omega) are -0.6, -0.6, -0.6 at zero degrees of attack, while these values are respectively. -7, -11 and -8.8 at 10 degrees of attack values while at 20 degrees angle of attack, -5.4, -5.8 values were obtained.

For NACA 65-421, the minimum static pressure coefficient values were -0.9, -0.9, -0.8 at zero-degree angle of attack (S-A, k-epsilon, k-omega) and -3.2, -3.5, -4 at 10-degree angle of attack and -7.4, -6.4, -6.4 values

respectively at 20 degrees angle of attack. Although this coefficient is affected by the angle of attack, it can be said that while the airfoil has negative values in almost all of its upper surface, it takes positive values in most of the lower surface.

In relation to the Bernoulli equation, different velocities around the airfoil generate a varied pressure distribution at each position around the body. The area on the upper surface rises as the cross section is bent, increasing the speed of the air traveling through the cross section. In comparison to the Bernoulli equation, as air velocity increases, pressure decreases much more.

The change in velocity in the flow around the airfoil can be represented by the map shown in a different colour. Similarly, the static pressure change can be shown by the colour change. Red colours represent the highest values, while blue colours represent the lowest values. Other colours represent values in this range. Table 4 compares the pressure contours of the airfoils for the three attack angles. The blue areas on the figures in the table show where the static pressure is low, while the green, yellow, and red sections show where the static pressure is higher than the blue zone.

**Table 4.** Pressure contour figures of the airfoils.

| **Pressure Contour** | **NACA 63-215** | **NACA 65-421** |
|---|---|---|
| **0° Spalart-Allmaras** | 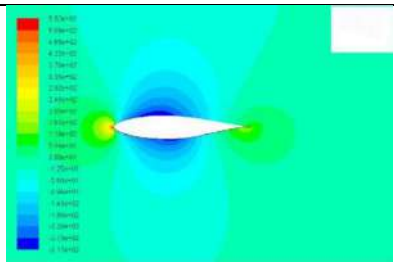 | 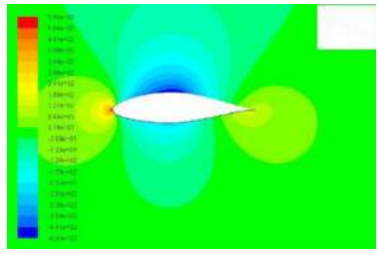 |
| **0° k-ε** | 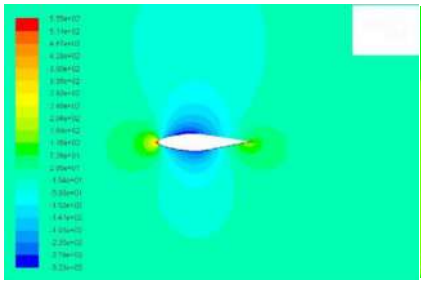 | 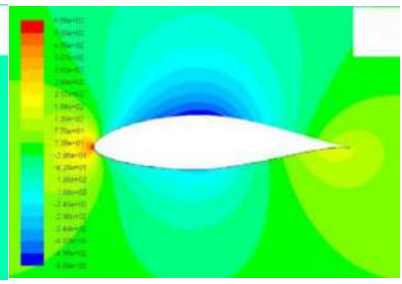 |

**0° k-ω**

**10° Spalart-Allmaras**

**10° k-ε**

**10° k-ω**

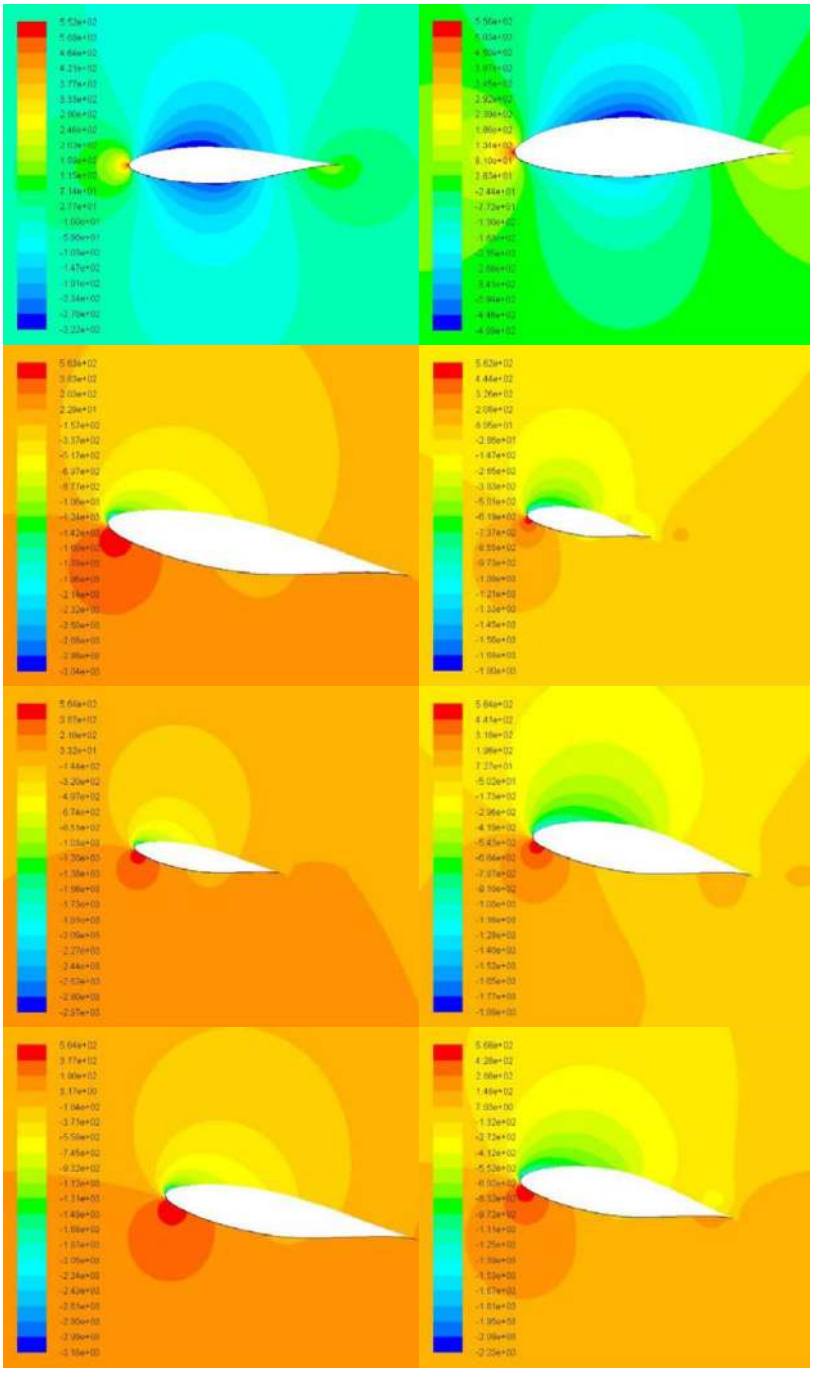

**20° Spalart - Allmaras**

**20° k-ε**

**20° k-ω**

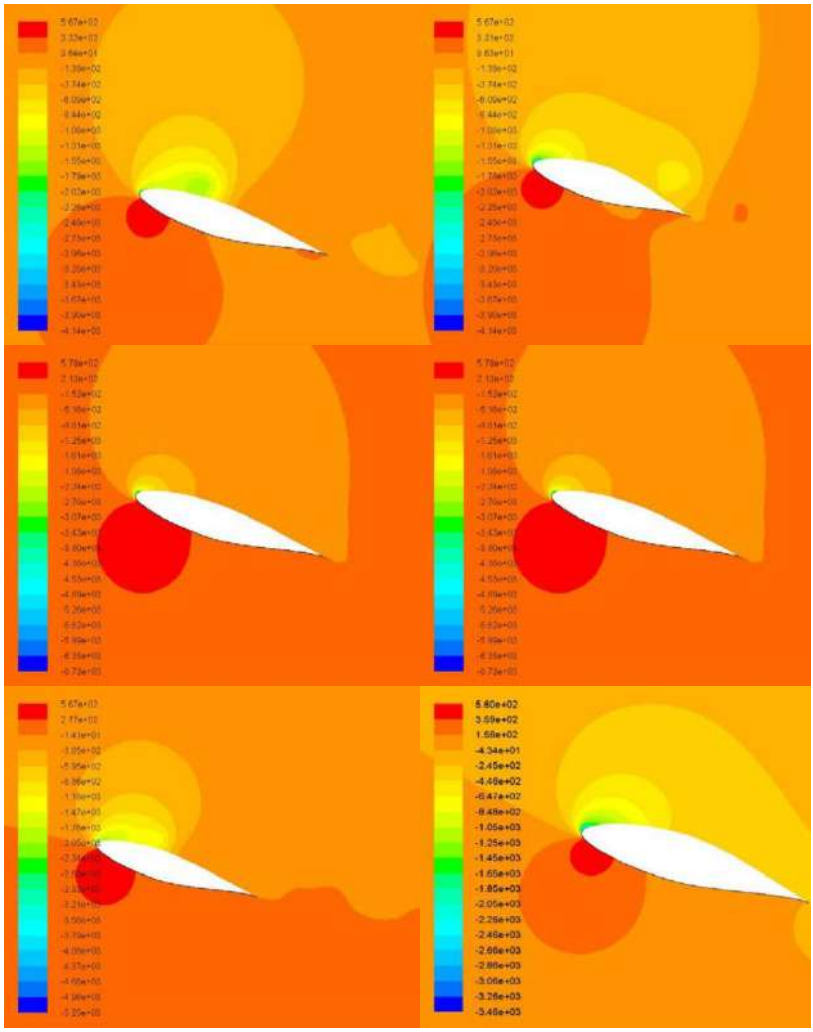

The static pressure is shown in red in Table 4 at the front tip of the airfoil sections because the flow velocity is zero at this location, as shown in Table 5, and the static pressure achieves its maximum value. The color of the region under the airfoil changes from blue to yellow as the attack angle increases. This variation is perceived as a rise in static pressure, and hence an increase in pressure differential and lift force.

When the pressure contours are carefully examined, it can be seen that there are slight differences between the turbulence models and the results. At zero-degree angle of attack, the minimum static effective pressure value obtained on the NACA 63-215 airfoil was calculated as -317 pascals in the Spalart-Allmaras turbulence model, -325 pascals in the k-epsilon

turbulence model and -322 pascals in the k-omega turbulence model. These values were calculated as -493 pascals, -509 pascals and -498 pascals for the Spalart-Allmaras, k-epsilon, k-omega turbulence models for NACA 65-421 airfoil, respectively. Maximum static pressure values were almost the same with all three turbulence models; For NACA 63-215, 555 pascals were obtained with Spalart-Allmaras, while 552 pascal values were obtained with k-epsilon and k-omega. The maximum (positive) effective static pressure value obtained in the NACA 65-421 airfoil was calculated as the same value, 556 pascals, with all three turbulence models.

Considering the pressure contours at 10 degrees angle of attack, the results obtained with the Spalart Allmaras, k-epsilon, k-omega turbulence models were as follows, respectively; Minimum static effective pressure values of -3044 pascal, -2970 pascal and -2430 pascal were obtained in NACA 63-215 airfoil. The maximum static effective pressure values obtained in the same airfoil were 563 pascals, 564 pascals and 564.4 pascals, respectively. Although there is a difference in the minimum values, it is understood that the maximum values are almost the same. Similarly, for the NACA 65-421 airfoil; The minimum pressure values obtained by turbulence models were -1800 pascals, -1834 pascals and -2230 pascals, respectively, while the positive pressure values were 562 pascals, 564 pascals, and 568 pascals, respectively.

While the negative pressure values obtained at 20 degrees angle of attack were obtained in the same turbulence order (SA, k-epsilon, k-omega) in NACA 63-215, -4140 pascals, -6720 pascals, -5250 pascals, in NACA 65-421 airfoil these values were respectively (SA, k-epsilon, k-omega) -4140 pascals, -5270 pascals, -3450 pascals were determined. Positive static pressure values, on the other hand, were the same as 567 pascals with all three turbulence models in NACA 63-215, slightly different values were obtained with three different turbulence models in the NACA 65-421 airfoil; if expressed in the same turbulence order; these values were 567 pascals, 558 pascals and 560 pascals.

In general, it can be said that in the calculation of positive pressure values, very close values are obtained with turbulence models. However, significant differences were observed in obtaining negative static pressure values. When the two airfoils are compared, it can be said that there is not much difference in terms of positive static pressure values, but there are significant differences in negative static pressure values.

At the point where the air approaching the airfoil first contacts the airfoil, the velocity is zero and the static pressure is at its maximum value, this point is called the stagnation point. The location of the stagnation points for the different angle of attacks are shown in Figure14.

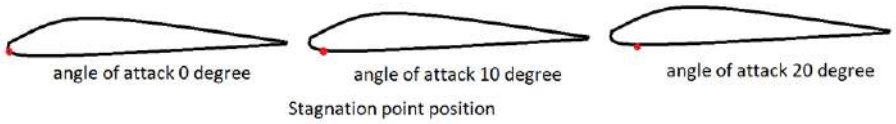


**Figure 14.** Position of the stagnation point varying with angle of attack

While the stagnation point is on the leading edge of the airfoil at zero degrees of attack, it can be observed from the static pressure contours (dark red zone) that this point is displaced towards the trailing edge at the lower surface of the airfoil by approximately 5% chord at 10 degrees attack angle and approximately 10% chord at 20 degrees attack angle.

Maximum velocity of the air particles moving over the airfoil result in minimum static pressure. The region that has high velocity around the airfoil changes with angle of attack. This is shown in Figure 15.

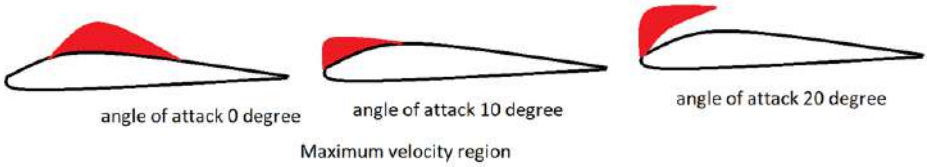


**Figure 15.** Position of the maximum velocity region varying with angle of attack

Finally, Table 5 compares the velocity contours of the airfoils for each of the three attack angles. The figures show that where flow separation occurs, the region becomes bluer and darker, and the velocity approaches zero.

**Table 5.** Velocity contour figures of the airfoils.

| Velocity Contour | NACA 63-215 | NACA 65-421 |
|---|---|---|
| 0° Spalart-Allmaras | 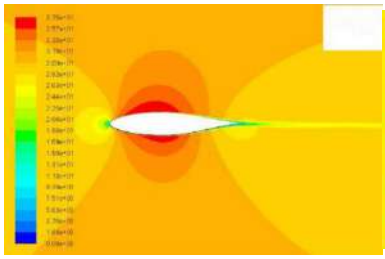 | 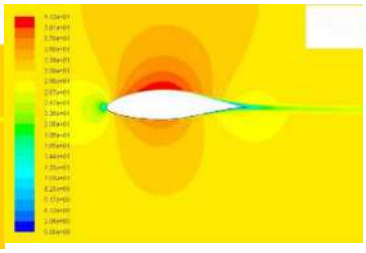 |
| 0° k-ε | 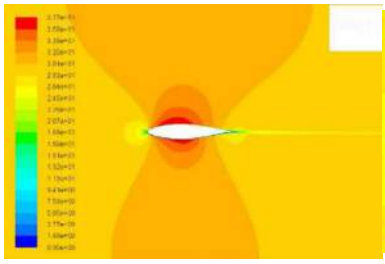 | 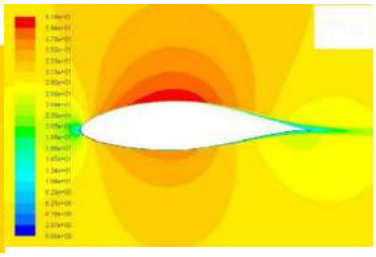 |
| 0° k-ω | 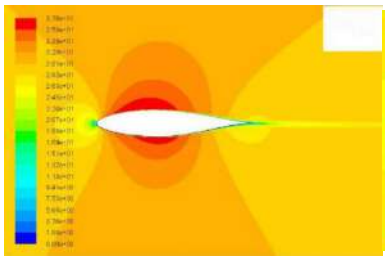 | 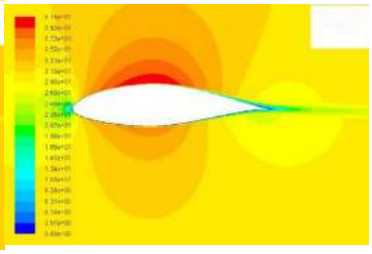 |
| 10° Spalart-Allmaras | 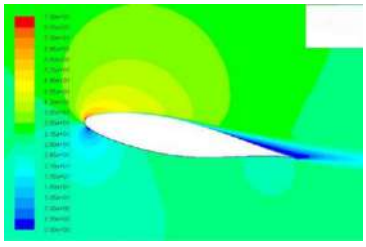 | 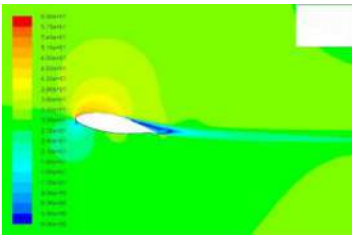 |

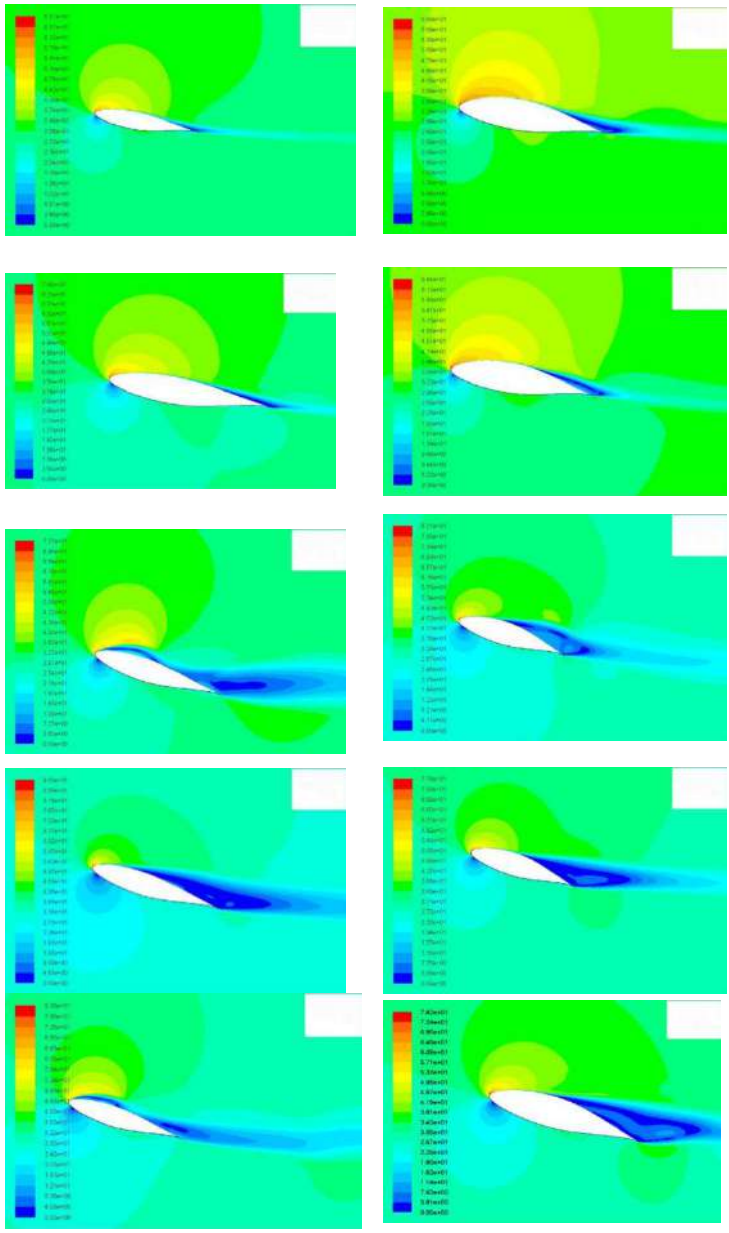


Looking at the velocity contours, it can be easily seen that the velocity of the air increases as it passes over the upper surface of the airfoil (dark red areas). At zero-degree angle of attack, the values of the maximum velocity found by turbulence models (S-A, k-epsilon, k-omega) in NACA 63-215 were obtained as 37.5 m/s, 37.7 m/s, and 37.6 m/s, respectively.

The same values were obtained for the NACA 65-421 airfoil as the maximum velocity values of 45.2 m/s, 41.4 m/s, and 41.3 m/s, respectively. It is seen from the contours that the maximum speed values increase when the angle of attack is increased to 10 degrees. At 10 degrees angle of attack, the maximum velocity values for NACA 63-215 in the order of turbulence models (S-A, k-epsilon, k-omega) are 70 m/s, 68 m/s, 70.8 m/s, while these values for NACA 65-421 are 60 m/s, 56 m/s, 64.4 m/s respectively. While at 20 degrees angle of attack, maximum speed values of 72.2 m/s, 90.5 m/s, 80.6 m/s were obtained in NACA 63-215 in the same order of turbulence, while these values were 82 m/s, 77.6 m/s, 76.2 for NACA 65-421, respectively.

It is understood from the speed contours that maximum speed values occur at NACA 65-421 at low angles of attack, while maximum speed values occur at NACA 63-215 at high angles of attack. In addition, in both airfoils, it can be said by looking at the contours that the maximum speed region shifts from the upper middle region of the airfoil towards the leading edge with the increase in the angle of attack.

The NACA 63-215 airfoil, with its low camber and thickness, is well-suited for aircraft wings that require low drag and good lift characteristics, such as light general aviation aircraft, gliders, and UAVs. NACA 65-421 airfoil, on the other hand, has a higher camber and thickness compared to NACA 63-215 airfoil, which makes it more suitable for aircraft that require higher lift, such as transport aircraft and some military aircraft. This airfoil has also been used in wind turbine blades, where its high lift-to-drag ratio makes it a good choice for low-speed wind energy conversion. While these airfoils are primarily designed for subsonic flow applications, they may still be used in transonic flows with proper design considerations. However, they are not suitable for supersonic flow applications.

## 5. Conclusion

The experimental results were correlated with the estimated coefficients of lift and drag powers. Both turbulence models before and after the stall angle indicated a considerable discrepancy with the experimental data, with the anticipated drag force being greater than the real data.

The static pressure distribution was illustrated on these two airfoils. At the same angle of attack, it was determined that NACA 63-215 had less negative pressure on the upper surface than NACA 65-421.

The main goal of this simulation was to evaluate the different characteristics of the NACA 63-215 and NACA 65-421 airfoils for the different turbulence models and with experimental data available in the literature to determine which model is the most efficient.

The study used the Spalart-Allmaras, turbulence standard k-ε turbulence, and standard k-ω turbulence models. The basic k-ω model is optimized for boundary layer flows and separation, but it does not reliably estimate coefficients of lift and drag in the far domain free-stream regions beyond the shear layer due to the solution's sensitivity to k values and ω in the free flow regions beyond the shear layer. Aside from that, k-ω; k-ε exhibits a better agreement with experimental data. However, it loses its balance following a stall argument. The Spalart-Allmaras turbulence model is found to produce a more accurate estimation of lift and drag coefficients in both the pre-stall and post-stall areas when compared to the other models.

The suitability of an airfoil for a particular vehicle or application depends on several factors, such as the desired lift and drag characteristics, the operating conditions, and other design considerations. Therefore, the selection of an appropriate airfoil should be made based on a thorough analysis of the specific application requirements. Both airfoils have similar aerodynamic properties, such as a low drag coefficient and a high lift-to-drag ratio. However, the NACA 63-215 airfoil has a higher critical Mach number and is more suitable for high-speed flight, while the NACA 65-421 airfoil has a higher lift coefficient and is more suitable for lower speed flight. As a continuation of this study, the aerodynamic performances of other airfoils can be calculated in a similar way. The lift and drag force coefficient values of symmetrical cambered airfoils can be compared.

In recent years, significant progress has been made in improving the accuracy and reliability of CFD simulations for airfoil aerodynamics. One major area of research is the development of more accurate and computationally efficient turbulence models, particularly in LES (Large Eddy Simulation) and DES (Detached Eddy Simulation). Additionally, advances in high-performance computing and meshing techniques have enabled more complex and detailed simulations, allowing for better understanding of the complex flow physics around airfoils**.**

The future of airfoil aerodynamics by CFD is likely to involve further advances in turbulence modelling, meshing techniques, and high-performance computing. Additionally, researchers are exploring the use of

machine learning and artificial intelligence techniques to improve the accuracy and speed of CFD simulations. These advances are expected to lead to the development of even more efficient and innovative airfoils.

**References**

[1] Anderson Jr., J.D. (2001). "Fundamentals of Aerodynamics", McGraw-Hill Education, New York.

[2] Abbot, I.H. and Von Doenhoff, A. E. (1959). "Theory of wing sections, Including a summary of airfoil data", Dover Publications Inc., New York, USA.

[3] Anderson J. D. (1995). "Computational Fluid Dynamics", McGraw-Hill, USA.

[4] Sarada, S., Shankar, M. S., Rudresh, G. (2010). "Numerical Simulation of Viscous, In-compressible Flow Around NACA64618 Subsonic Airfoil using Computational Fluid Dynamics", Proceedings of National conference on advances in Mechanical Engineering, India.

[5] Saraf, A., Nazar, F. A., Singh, S. P. (2012). "Analysis of the k-ϵ and k-ω Standard Models for the Simulation of the Flow Over a National Advisory Committee for Aeronautics (NACA) 4412 Airfoil", International Journal of Scientific & Engineering Research, India.

[6] Hartwanger, D., Horvat, A. (2008). "3D modeling of a Wind Turbine using CFD", NAFEMS Conference, United Kingdom.

[7] Ravi, H. C., Madhukeshwara, N., Kumarappa, S. (2013). "Numerical Investigation of Flow Transition for NACA-4412 Airfoil using Computational Fluid Dynamics, International Journal of Innovative Research in Science", Engineering and Technology, India.

[8] Eleni, D. C., Athanasios, T. I., Dionissios, M. P. (2012). "Evaluation of the Turbulence Models for the Simulation of the Flow over an Aerofoil", Journal of Mechanical Engineering Research, Greece.

[9] Johansen J. (1997). "Prediction of Laminar/Turbulent Transition in Airfoil Flows", Journal of Aircraft, Aerospace Research Central, Denmark.

[10] Launder, B. E. & Spalding D. B. (1974). "The Numerical Computation of Turbulent Flows", Computer Methods in Applied Mechanics and Engineering, ScienceDirect, United Kingdom.

[11] Gulzar, O., Gulzar, S., Bhatele, S., Soni, N. (2014). "Impact of Variation in Angle of Attack on NACA7420 Airfoil in Transonic Compressible Flow Using Spalart-Allmaras Turbulence Model", IJRMET, India.

[12] Kumar, B. N., Paramasivam, K. M., Prasanna, M., Karis, M. (2016). "Computational Fluid Dynamics Analysis of Aerodynamic Characteristics of NACA 4412 vs S809 Airfoil for Wind Turbine Applications", International Journal of Advanced Engineering Technology, India.

[13] Badran, O. (2008). "Formulation of Two-Equation Turbulence Models for Turbulent Flow over a NACA 4412 Airfoil at Angle of Attack 15 Degree", Proceedings of 6th International Colloquium on Bluff Bodies Aerodynamics and Applications, Italy.

[14] Hassan, G. E., Hassan, A., Youssef, M. E. (2014). "Numerical Investigation of Medium Range Re Number Aerodynamics Characteristics for NACA0018 Airfoil", CFD letters, Egypt.
[15] Smyth, Thomas AG. "A review of Computational Fluid Dynamics (CFD) airflow modelling over aeolian landforms", Aeolian Research 22 (2016): 153-164.
[16] Hansen, M.O.L. and Sørensen, N.N. (2004). "Aerodynamics of Wind Turbines", 2nd Edition. Earthscan, London.
[17] Wilcox, C. D. (1993). "Turbulence Modelling for CFD, DCW Industries", library copy, USA.
[18] N. K. Anand and C. L. Streett, "A comparative study of turbulence models in predicting flow over a NACA 0012 airfoil", Journal of Aircraft, vol. 48, no. 1, pp. 207-214, January-February 2011.
[19] R. L. Spalart and S. R. Allmaras, "A one-equation turbulence model for aerodynamic flows", AIAA Paper 92-0439, January 1992.
[20] Spalart, P.; Allmaras, S. (1992). "One-equation turbulence model for aerodynamic flows", 30th Aerospace Sciences Meeting and Exhibition, AIAA. doi: 10.2514 / 6.1992-439.
[21] Fluent Inc, (2006). "Standard and SST – k-epsilon Models Theory", FLUENT 6.3 User's Guide,
[22] Menter, FR (1994). "Two-Equation Eddy-Viscosity Turbulence Models for Engineering Applications", AIAA Journal. 32 (8): 1598-1605. doi : 10.2514 / 3.12149
[23] Spalart, P. R., Allmaras S. R. (1992). "A One-Equation Turbulence Model for Aerodynamic Flows", AIAA Paper, USA.
[24] Launder, B.E. and Spalding, D.B. (1972). "Lectures in Mathematical Models of Turbulence", Academic Press, London.
[25] Sahin, I & Acir, A. (2015). "Numerical and Experimental Investigations of Lift and Drag Performances of NACA 0015 Wind Turbine Airfoil", International Journal of Materials, Mechanics and Manufacturing, Turkey.
[26] Hanjalic, K.; Laundering, B. (1972). "A Reynolds stress model applying to turbulent and fine shear flows". Journal of Fluid Mechanics. 52(4): 609–638. doi: 10.1017 / S002211207200268X
[27] Sørensen, N.N. and Mygind, L. (2001). "Airfoils for Wind Turbine Applications", Risø National Laboratory, Roskilde.
[28] Shih, T.H., Liou, W.W., Shabbir, A., Yang, Z., and Zhu, J. (1995). "A new k-epsilon eddy viscosity model for high Reynolds number turbulent flows", Computers & Fluids, 24(3), 227-238.
[29] Chan, T. L., Dong, G., Leung, C. W. Cheung, C. S., Hung, W. T., (2002). "Validation of a two-dimensional pollutant dispersion model in an isolated street canyon", Atmospheric Environment, Hong Kong, China.